*Q. J. R. Meteorol. Soc.* (2004), **130**, pp. 2217–2232 doi: 10.1256/qj.03.136

# Estimating the direct aerosol radiative perturbation: Impact of ocean surface representation and aerosol non-sphericity

By N. BELLOUIN*, O. BOUCHER, M. VESPERINI and D. TANRÉ
*Laboratoire d'Optique Atmosphérique, Université des Sciences et Technologies de Lille, Villeneuve d'Ascq, France*

(Received 30 July 2003; revised 12 March 2004)

SUMMARY

Atmospheric aerosols are now actively studied, in particular because of their radiative and climate impacts. Estimations of the direct aerosol radiative perturbation, caused by extinction of incident solar radiation, usually rely on radiative transfer codes and involve simplifying hypotheses. This paper addresses two approximations which are widely used for the sake of simplicity and limiting the computational cost of the calculations. Firstly, it is shown that using a Lambertian albedo instead of the more rigorous bidirectional reflectance distribution function (BRDF) to model the ocean surface radiative properties leads to large relative errors in the instantaneous aerosol radiative perturbation. When averaging over the day, these errors cancel out to acceptable levels of less than 3% (except in the northern hemisphere winter). The other scope of this study is to address aerosol non-sphericity effects. Comparing an experimental phase function with an equivalent Mie-calculated phase function, we found acceptable relative errors if the aerosol radiative perturbation calculated for a given optical thickness is daily averaged. However, retrieval of the optical thickness of non-spherical aerosols assuming spherical particles can lead to significant errors. This is due to significant differences between the spherical and non-spherical phase functions. Discrepancies in aerosol radiative perturbation between the spherical and non-spherical cases are sometimes reduced and sometimes enhanced if the aerosol optical thickness for the spherical case is adjusted to fit the simulated radiance of the non-spherical case.

KEYWORDS: BRDF Radiative transfer Saharan dust

## 1. INTRODUCTION

Aerosols affect the atmospheric solar radiation through scattering and absorption. This causes a change in the spectral and angular distribution of radiation in the atmosphere. We refer to the change in net radiation as the direct aerosol radiative perturbation (DARP). It is termed radiative forcing when only anthropogenic aerosols are considered. Numerical methods used to estimate this direct effect evolved throughout the 1990s. Charlson *et al.* (1992) estimated the DARP using an approximated, analytical equation based on aerosol optical thickness (AOT) and hemispheric upscatter fraction. A more general formulation, accounting for aerosol absorption through the aerosol single-scattering albedo, was proposed by Haywood and Shine (1995) and Chylek and Wong (1995). Dependence of the DARP on solar zenith angle (SZA, $\theta_s$) was introduced by Russell *et al.* (1997). Similarly, surface modelling evolved from an albedo independent of SZA (Charlson *et al.* 1992) to a surface albedo varying with the SZA (Russell *et al.* 1997) in the case of an oceanic surface. Radiative transfer codes solving numerically the radiative transfer equation replace these simplified equations. Intercomparison of the DARP for non-absorbing aerosols showed a general agreement among different codes of varying complexity although discrepancies ($\pm$ 20%) were also observed (Boucher *et al.* 1998).

Calculations of the DARP usually rely on the assumption of a Lambertian surface. New radiative transfer codes allow the use of a bidirectional reflectance distribution function (BRDF) to characterize the radiative behaviour of the surface. Although more rigorous than using a SZA-dependent albedo, the considerable increase in computer time associated with the BRDF use prevents routine usage. Therefore, the impact of using a

* Corresponding address: Laboratoire d'Optique Atmosphérique, Bâtiment P5, USTL, 59655 Villeneuve d'Ascq Cedex, France. e-mail: bellouin@loa.univ-lille1.fr

simplified surface model instead of a BRDF for an oceanic surface is addressed in this study.

Mie theory describes scattering by spherical particles. Most aerosols, especially in the coarse mode, are non-spherical, thus preventing use of the Mie theory to calculate their optical properties. Theoretical calculations have been done using particles built on Chebyshev polynomials (Mugnai and Wiscombe 1986, 1989; Wiscombe and Mugnai 1988), spheroids (Mishchenko *et al.* 1996), and convex or concave particles (Yang *et al.* 2000). However most radiative transfer calculations remain based on Mie theory for the sake of simplicity and computer-time issues. Previous numerical studies by Mishchenko *et al.* (1995, 1997) showed that satellite-based remote sensing of aerosols based on Mie theory would cause significant errors in the retrieved AOT if aerosols were spheroids. However, if the AOT is already known, the impact of non-sphericity on the local albedo is smaller. Moreover, errors do not cancel out if Mie theory is used to invert measured radiances and to calculate the DARP. Pilinis and Li (1998), using a box model, showed that assuming homogeneous spherical aerosols instead of non-spherical ones may introduce large errors in DARP estimations. Zhao *et al.* (2003) and Wang *et al.* (2003) showed that considering aerosol non-sphericity significantly improves satellite retrievals of the AOT. Using previously published experimental measurements of the phase function of non-spherical aerosols (Volten *et al.* 2001), this paper quantifies the impact of neglecting non-sphericity effects in simulations of the DARP.

## 2. Impact of modelling the surface radiative properties

### (*a*) *Radiative transfer code*

The Streamer radiative code (Key and Schweiger 1998) is based on the discrete-ordinate method (Stamnes *et al.* 1988) which allows, in its latest version, the use of a surface BRDF or the albedo of a Lambertian surface. Fluxes are integrated over 24 short-wave bands, ranging from 0.28 to 4 $\mu$m. Calculations are made using 24 streams, with gaseous absorption included. It has been checked that the Streamer model produces exactly the same results whether a given Lambertian albedo is prescribed through a constant BRDF or through the albedo option of the code. This precludes the differences between our surface BRDF and albedo simulations from being a numerical artefact.

### (*b*) *Aerosol radiative perturbation calculation*

We adapted three different aerosol types, represented by three different bimodal log-normal particle volume distributions and absorption properties, from Dubovik *et al.* (2002). Their parameters are summarized in Table 1. The dust model from Cape Verde represents coarse-mode aerosol with little absorption. The pollution model from Maryland and the biomass-burning model from Zambia consist of smaller aerosols, with small and high absorption, respectively. For each model, Mie calculations are used to estimate the spectrally-varying (i) aerosol extinction coefficient, (ii) single-scattering albedo, which is the ratio of scattering to extinction, and (iii) phase function, which is truncated and decomposed in 48 Legendre moments. Those parameters are used as inputs to the Streamer radiative code. Another parameter of interest is the upscatter fraction for monodirectional radiation, $\beta(\theta_s)$, which, although not used directly in the calculations, is helpful to interpret the results. It is defined as the fraction of direct radiation with SZA $\theta_s$ scattered by the aerosol into the upward hemisphere (Wiscombe and Grams 1976; Boucher 1998).

The DARP, $\Delta F(\theta_s)$, is defined for a SZA $\theta_s$ as the difference in net (downward minus upward) short-wave flux with and without aerosols. Here we focus on the aerosol

TABLE 1. PARAMETERS OF THE THREE BIMODAL LOG-NORMAL AEROSOL MODELS USED IN ESTIMATING THE IMPACT OF THE SURFACE REPRESENTATION

| | Dust | Pollution | Biomass burning |
|---|---|---|---|
| $r_{0a}$ | 0.12 | 0.12 | 0.12 |
| $r_{0c}$ | 1.90 | 3.03 | 3.22 |
| $\sigma_{0a}$ | 0.49 | 0.38 | 0.40 |
| $\sigma_{0c}$ | 0.63 | 0.75 | 0.73 |
| $C_{va}$ | 0.02 | 0.02 | 0.12 |
| $C_{vc}$ | 0.90 | 0.02 | 0.09 |
| $\Re(m)$ | 1.48 | 1.41 | 1.51 |
| $\Im(m)$ | 0.0007 | 0.003 | 0.021 |
| $\varpi_0$ | 0.98 | 0.94 | 0.77 |
| $g$ | 0.70 | 0.54 | 0.47 |
| $\alpha$ | 0.00 | 1.56 | 1.77 |

$r_0$ ($\mu$m) and $\sigma_0$ are the modal radius and standard deviation of the log-normal distribution of aerosol volume in each mode.
$C_v$ is the particle volume concentration.
Subscripts a and c denote the accumulation and coarse modes, respectively.
$m$ is the complex refractive index at 865 nm.
The single scattering albedo, $\varpi_0$, and the phase function asymmetry factor, $g$, result from Mie calculations at 865 nm.
$\alpha$ is the Ångström exponent calculated between 670 and 865 nm.

radiative perturbation at the top of the atmosphere (TOA). Results at the surface differ in magnitude, mainly because of aerosol absorption, but the qualitative interpretation remains the same. For a given atmospheric level and AOT, the magnitude of the DARP is directly related to the aerosol phase function; large aerosols have a sharp forward peak, thus a low upscatter fraction and radiative perturbation. Figure 1 shows the DARP of our three aerosol models at an AOT of 0.1 and 0.5 at 865 nm. The surface is modelled by its BRDF. The DARP exhibits a minimum (or maximum in absolute values) at some intermediate SZAs, eventually reaching 0 W $m^{-2}$ at a SZA of 90° (Nemesure *et al.* 1995; Boucher *et al.* 1998). This minimum results from the competition between aerosol and Rayleigh scattering. The minimum shifts towards small SZAs if aerosol upscatter is weak, which occurs in the case of large aerosols (dust model) and/or large aerosol absorption (biomass-burning aerosol). In contrast, if aerosol upscatter is large, the minimum moves to larger SZAs. This is the case for small aerosols (pollution or biomass-burning aerosols) but also small AOT and/or bright surfaces (which enhances upward fluxes).

### (*c*) *Surface representation*

Radiative transfer in the atmosphere requires the knowledge of the surface optical properties which can be described through an albedo or a BRDF. Surface albedo is defined as the ratio between the reflected upward and downward fluxes. This quantity thus depends on the way the surface is illuminated, which relates to the SZA as well as atmospheric scattering and absorption. In contrast to surface albedo, the BRDF is an intrinsic property of the surface and does not depend on the way it is illuminated. The BRDF gives the fraction of reflected radiation for each combination of incident and reflection geometry. For a given viewing geometry it can be considered as the albedo of the surface, should it reflect radiation in the same way in the other directions.

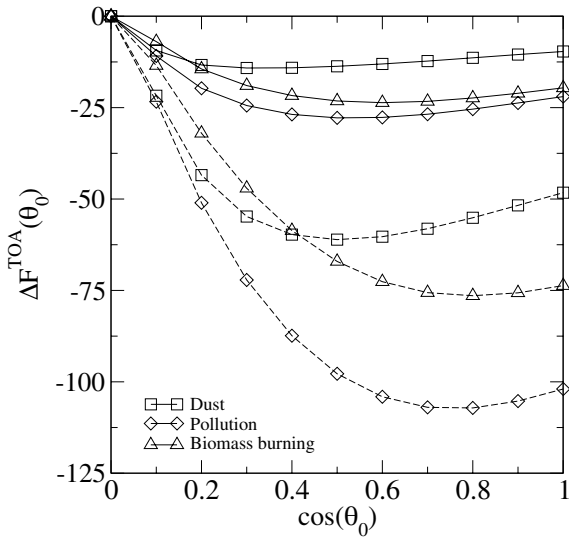


Figure 1. Aerosol radiative perturbation (W $m^{-2}$) estimated at the top of the atmosphere for our three different aerosol models (see Table 1). The aerosol optical thickness is 0.1 (solid lines) and 0.5 (dashed lines) at 865 nm.

Here we focus on the open ocean surface, which was chosen for three reasons: (i) ocean covers about two thirds of the earth's surface, (ii) aerosol properties can be accurately retrieved from space over the ocean, and (iii) the ocean BRDF is very anisotropic so the effects of anisotropy found here probably represents an upper bound. The oceanic BRDF is calculated following Cox and Munk (1954) as the Fresnel reflection function weighted by the wave slope probability. Wind speed is taken as constant at 7 m $s^{-1}$.

Using the BRDF of the ocean coupled with an aerosol model, one can compute the upward and downward fluxes in the atmosphere and at the surface. The ratio of these two fluxes at the surface is the actual surface albedo which depends on the aerosol content through its impact on the shape of the incident radiation field. This albedo is used in a second estimation of the fluxes with the Lambertian surface assumption. The DARP can be estimated as the difference between upward fluxes with and without aerosols, as illustrated in Fig. 2.

### (*d*) *Results*

Fig. 3 shows the effect of aerosols on the surface albedo as computed in our BRDF-case simulations. The choice of the dust model is to get the largest impact on the surface albedo. The case without aerosols shows the usual increase in surface albedo due to Fresnel reflection as SZA increases, up to 0.14 for $\cos(\theta_s) = 0.1$. In this case, the angular distribution of the downward radiation gathers around the SZA in a tight cone. When aerosols are present, surface albedo is increased and decreased at small and large SZA, respectively. This can be explained by a change in the angular distribution of downward radiation, which broadens due to multiple scattering caused by the increase in the AOT. For very large AOTs, the distribution of radiation is more isotropic, which flattens the dependence of surface albedo on the SZA. The reduction in surface albedo at large SZA can be very large (up to a factor of 3) for an AOT at 865 nm of 0.5.

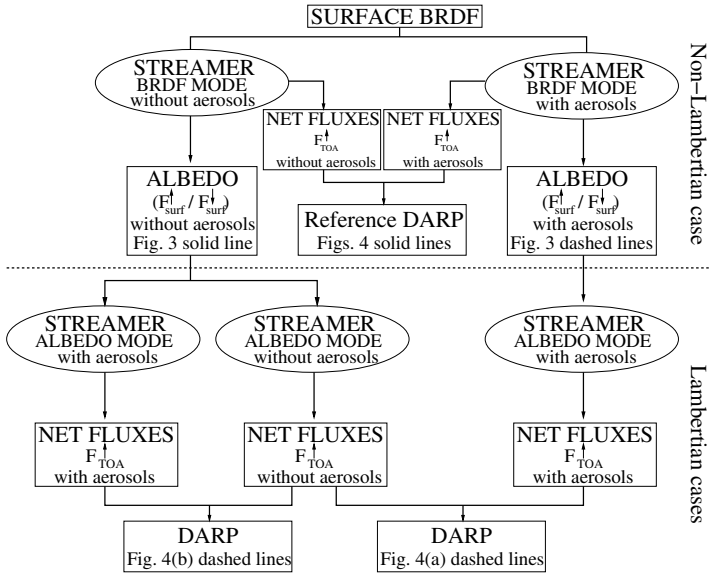


Figure 2. Schematic of radiative transfer calculations performed to study the impact of the oceanic surface representation. STREAMER is the radiative transfer code used in this study. Upward and downward net fluxes are $F^{\uparrow}$ and $F^{\downarrow}$, respectively, while subscripts 'surf' and 'TOA' denote the surface and top of atmosphere, respectively.

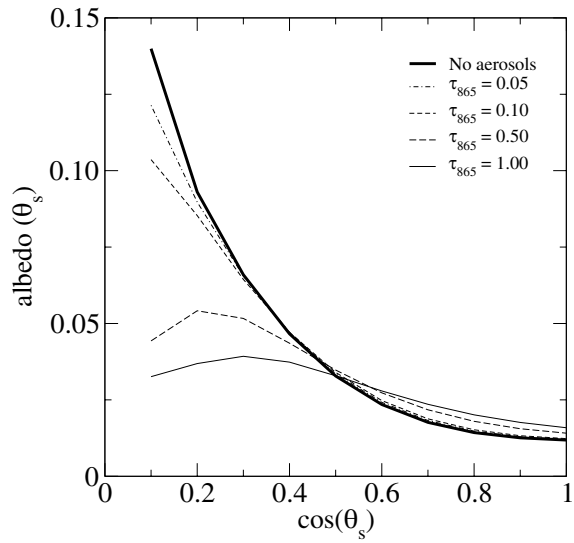


Figure 3. Short-wave albedo of the oceanic surface as a function of the cosine of the solar zenith angle. The thick solid line is the reference case, calculated with no aerosol included. The other lines represent increasing optical thicknesses at 865 nm for the dust aerosol model.

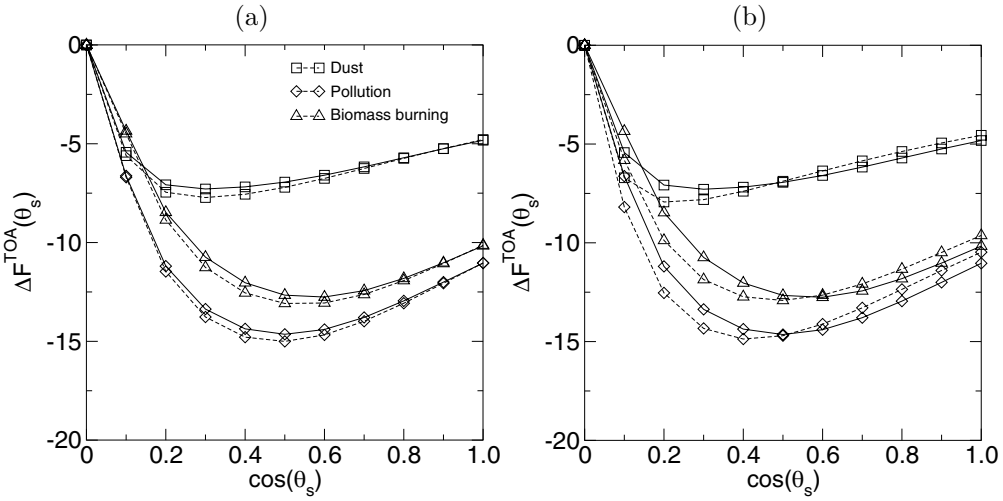


Figure 4. Aerosol radiative perturbation (W $m^{-2}$) estimated at the top of atmosphere for three different aerosol models and an aerosol optical thickness at 865 nm of 0.05. The surface is modelled through a surface albedo (dashed line) or through the real surface bidirectional reflectance distribution function (BRDF, solid line). The surface albedo in the Lambertian case with aerosol is that of the BRDF case with aerosol in (a) and no aerosol in (b). See text and Fig. 2 for further explanation.

Fig. 4(a) shows the DARP at TOA as a function of the cosine of the SZA for a constant optical thickness at 865 nm of 0.05 for our three aerosol models. Such a small optical thickness has been chosen in order to get a large contribution of the surface to the total signal. As discussed in section 2(b), small particles induce a greater flux perturbation than large particles, because of their larger upscatter fraction. Absorption reduces significantly the radiative perturbation at the TOA, as can be seen from the comparison of the low-absorbing pollution and high-absorbing biomass-burning cases. Here the surface albedo for the Lambertian case is that of its non-Lambertian counterpart. Therefore, the Lambertian and non-Lambertian cases have exactly the same surface albedo which is different between the aerosol and non-aerosol cases. By doing so, estimates of the DARP in the Lambertian and non-Lambertian cases are very close to each other and exhibit a minimum for the same SZA. Lambertian and non-Lambertian lines intersect around $\cos(\theta_s) = 0.9$. Relative difference remains below 5% for all three models. However, the practical intent of this simplification is limited because the non-Lambertian (BRDF) calculation is required to get the Lambertian results. The computational burden is therefore not reduced.

For a faster computation, the Lambertian case calculations with aerosols can also be done by approximating the surface albedo to that of the aerosol-free atmosphere. These results are shown in Fig. 4(b). Although less rigorous, this method is more affordable in terms of computational cost as non-Lambertian calculations are needed only once (the no-aerosol case) for each SZA. Such an approximation leads to absolute relative errors of up to 25% as shown in Fig. 5(a). Errors are enhanced in the case of large aerosol absorption. For the dust model, Fig. 5(b) shows that the error is reduced in the case of multiple scattering due to large optical thickness. Relative errors are less than 7% for an AOT at 865 nm of 1. The errors are actually due to a shift in the position of the minimum of the DARP with SZA and therefore change sign at a SZA of about 60°. This can be interpreted by looking at the differences in surface albedo computed for the aerosol and no-aerosol cases (Fig. 3).

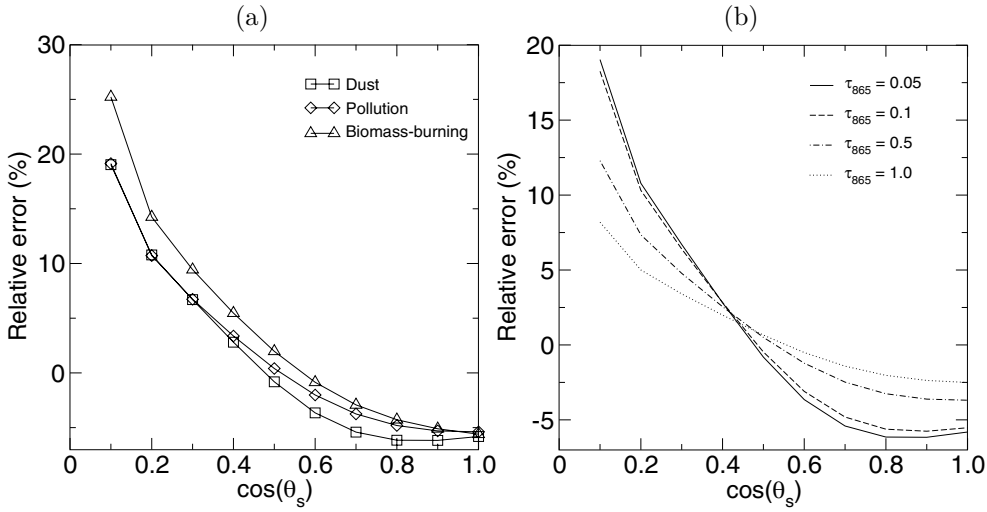


Figure 5. Relative difference (%) between the DARP estimated using non-Lambertian and Lambertian surfaces: (a) for the three aerosol models with an aerosol optical thickness at 865 nm of 0.05, (b) for the dust aerosol only and four increasing optical thicknesses. The Lambertian surface has the albedo of the no-aerosol case, as in Fig. 4(b).

TABLE 2. DAILY-AVERAGED RADIATIVE FORCING PERTURBATIONS, ESTIMATED WITH AN AEROSOL OPTICAL THICKNESS OF 0.05 AT 865 nm

| | | Equinox | | Solstices | | |
|---|---|---|---|---|---|---|
| Aerosol model | Surface model | 45°N spring/autumn | Equator | 45°N summer | Equator summer/winter | 45°N winter |
| Dust | Albedo | –3.28 | –2.92 | –3.88 | –3.02 | –2.55 |
| | BRDF | –3.19 | –2.91 | –3.83 | –2.99 | –2.31 |
| | | (2.7%) | (1.0%) | (1.3%) | (1.0%) | (10.4%) |
| Pollution | Albedo | –6.43 | –5.99 | –7.80 | –6.14 | –4.31 |
| | BRDF | –6.29 | –6.00 | –7.76 | –6.13 | –3.93 |
| | | (2.2%) | (–0.2%) | (0.5%) | (0.2%) | (9.7%) |
| Biomass burning | Albedo | –5.54 | –5.27 | –6.82 | –5.39 | –3.48 |
| | BRDF | –5.34 | –5.23 | –6.71 | –5.32 | –3.08 |
| | | (3.6%) | (0.8%) | (1.6%) | (1.3%) | (13.0%) |

Figures in parentheses indicate the percentage difference between the two surface representations.
No account is taken of changes in earth–sun distance with time of year.

The results presented so far are for the instantaneous (i.e. SZA-dependent) DARP. However, from a climate perspective, it is more interesting to consider the daily-averaged radiative perturbation, which requires an integration over SZAs. The distribution of SZA depends on day of the year and latitude. Table 2 presents the daily-averaged radiative perturbation for the spring equinox and summer and winter solstices, at the equator and 45°N. Surface albedo is estimated from the no-aerosol case. The error in daily-averaged DARP is reduced significantly if it is integrated over a large range of SZAs, as is the case at the equator or in midlatitude summer (see Table 2). However the error remains large if only large SZAs are considered in the integration, e.g. during midlatitude winter. Note also that the bias caused by the no-aerosol ocean albedo is almost always negative and therefore cannot be expected to cancel out when integrating seasonally and spatially.

## 3. Impact of non-sphericity of dust aerosols

In order to compare DARPs induced by spherical or non-spherical aerosols, two phase functions are needed. The non-spherical aerosol phase function is taken from Volten *et al.* (2001). Some missing features were added. The spherical aerosol phase function is calculated using Mie theory. We are then able to compare DARPs calculated using the two models at a given AOT. The impact of non-sphericity on AOT inversion from space measurements is also investigated, as well as the transfer of errors made on the AOT to the DARP.

### (*a*) *Aerosol phase functions*

Volten *et al.* (2001) measured the phase function of several randomly-oriented non-spherical mineral aerosols, including dust and volcanic ash. The device used, based on a laser, reaches scattering angles between 5° and 173°. The strong forward peak and the backscatter features are then not documented. These measurements, performed at 632.8 nm, produced results consistent enough to build an average aerosol phase function. This phase function allows a much better retrieval of dusty scenes from the angular and polarized information of the POLDER instrument (Deuzé *et al.* 2000; J.-L. Deuzé, personal communication). We therefore base our analysis of aerosol non-sphericity effects on this phase function.

Our first task was to extend the phase function to the full range of scattering angles. As forward scattering is dominated by diffraction, the shape of the particle is not important for scattering angles smaller than 5° and an equivalent spherical model can be assumed. We select the effective radius of 2.3 $\mu$m and effective standard deviation of 1.5 of the quartz sample studied by Volten *et al.* (2001). Such a size distribution is typical of dust atmospheric aerosol (e.g. Haywood *et al.* 2003). We further assume a refractive index $m = 1.55–0.0007i$, which is typical for Saharan measurements (Dubovik *et al.* 2002; Haywood *et al.* 2003). The phase function at backscattering angles (from 173° to 180°) is extrapolated from the sidescattering values, as it is expected that non-spherical particles exhibit no enhanced backscatter (Mugnai and Wiscombe 1989).

Fig. 6(a) presents the spherical and non-spherical phase functions as a function of scattering angle. It is interesting to note the large differences in sidescattering (scattering angles ranging from 60° to 140°) which corresponds to viewing geometries easily reached by space sensors. The better balance between forward and sidescattering of non-spherical aerosols enhances (decreases) the upscatter fraction at small (large) SZAs. The asymmetry parameters, $g$, of the spherical and non-spherical aerosol models are very close, 0.71 and 0.72 at 632.8 nm, respectively. This is due to the large weight of the forward peak in the calculation of $g$. Fig. 6(b) shows the upscatter fraction dependence on the cosine of the SZA for both shapes. Spherical particles upscatter more (less) than non-spherical particles for SZAs larger (smaller) than 45° (cosine 0.7). Because it is not trivial to derive the spectral dependence of our non-spherical dust model, we restrict hereafter all our flux calculations to the 0.57–0.64 $\mu$m waveband of the Streamer model.

### (*b*) *Impact of non-sphericity on the DARP: Constant AOT*

Radiative perturbations are calculated with the Streamer radiative code using the approximated Lambertian oceanic albedo (see bold solid line in Fig. 3). The reference AOT is taken at 865 nm; the AOT and single-scattering albedo at the Streamer waveband are taken from the Mie calculations for both models, so only the phase function differs in our calculations.

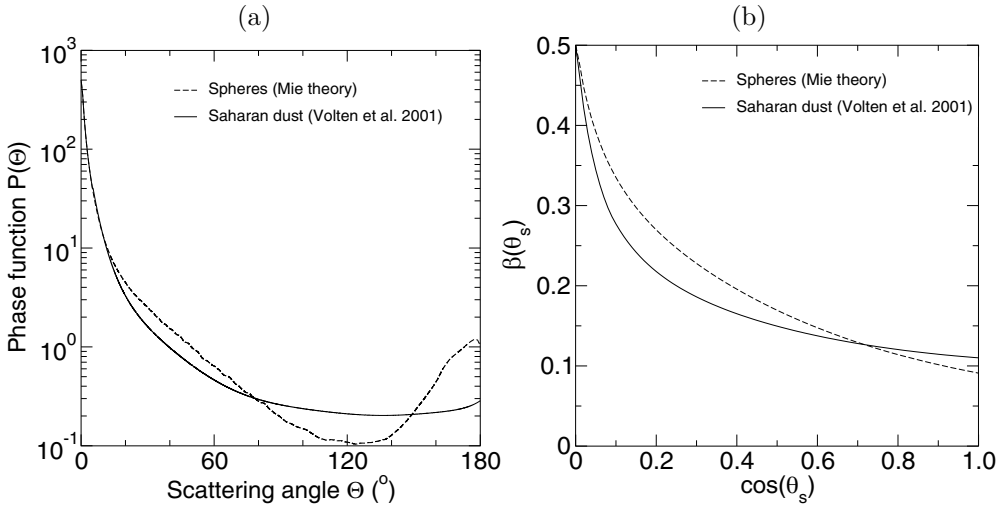


Figure 6. (a) Scattering phase function of non-spherical aerosols from Volten *et al.* (2001) (solid line) and corresponding spherical model (dashed line) at 632.8 nm as a function of the scattering angle. The forward peaks are assumed to be the same for the two phase functions. Both phase functions are normalized to $4\pi$. (b) Upscatter fraction as a function of the cosine of the solar zenith angle for the spherical and non-spherical cases.

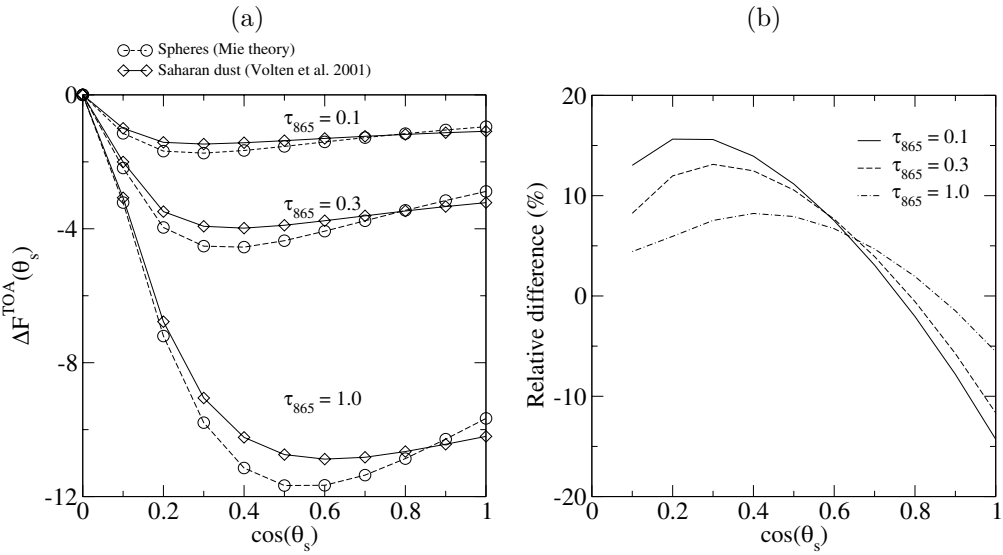


Figure 7. (a) Aerosol radiative perturbation (W $m^{-2}$) in the 0.57–0.64 $\mu$m waveband for the spherical and non-spherical cases and three different aerosol optical thicknesses at 865 nm. (b) Relative difference (%) between the two particle shapes considered.

Figure 7 presents the aerosol radiative perturbations in the 0.57–0.64 $\mu$m waveband and relative differences between the spherical and non-spherical models obtained at TOA for small, medium, and large AOTs. Qualitatively, for a given AOT, the aerosol radiative perturbation for the non-spherical model exhibits a less pronounced minimum at intermediate SZAs than the spherical model. The relative differences are large, greater

TABLE 3. DAILY-AVERAGED AEROSOL RADIATIVE PERTURBATIONS, ESTIMATED WITH VARYING AEROSOL OPTICAL THICKNESS AT 865 nm

| | | Equinox | | Solstices | | |
|---|---|---|---|---|---|---|
| Optical thickness | Aerosol model | 30°N spring/autumn | Equator | 30°N summer | Equator summer/winter | 30°N winter |
| 0.1 | Spherical | –0.66 | –0.61 | –0.72 | –0.64 | –0.61 |
| | Non-spherical | –0.61 | –0.60 | –0.69 | –0.60 | –0.54 |
| | | (7.6%) | (1.6%) | (4.2%) | (6.3%) | (11.5%) |
| 0.3 | Spherical | –1.81 | –1.72 | –2.00 | –1.77 | –1.63 |
| | Non-spherical | –1.67 | –1.70 | –1.94 | –1.69 | –1.45 |
| | | (7.7%) | (1.2%) | (3.0%) | (4.5%) | (11.0%) |
| 1.0 | Spherical | –4.87 | –4.80 | –5.53 | –4.85 | –3.96 |
| | Non-spherical | –4.69 | –4.65 | –5.39 | –4.67 | –3.67 |
| | | (3.7%) | (3.1%) | (2.5%) | (3.7%) | (7.3%) |

Figures in parentheses indicate the relative differences between spherical (Mie) and non-spherical (Volten) aerosols.
No account is taken of changes in earth–sun distance with time of year.

than 15% for an AOT at 865 nm of 0.1, reducing to less than 10% for an optical thickness of 1.0.

For daily-averaged radiative perturbation, relative differences decrease to reasonable values, as presented in Table 3. Calculations have been restricted to tropical latitudes (0–30°N), where non-spherical dust is a common aerosol type. For winter days at 30°N, when SZAs are large throughout the day, relative differences remain significant at more than 10% for medium aerosol loading. It is interesting to note that the distribution of SZA in the day always leads to a spherical aerosol DARP larger (in magnitude) than the non-spherical one.

### (*c*) *Impact of non-sphericity on retrieved AOT*

One of the major uses of remote sensing in the aerosol field is to retrieve the AOT from radiance measurements. Non-spherical particles exhibit large sidescattering, leading to significant errors in the AOT if the retrieval is based on Mie theory (Mishchenko *et al.* 1995). We re-evaluate here how non-spherical effects can affect the retrieval of the AOT.

We compute TOA radiances at 670 nm as a function of the AOT accounting for the various contributions of the surface and atmosphere (Tanré *et al.* 1983). The surface considered is that of the open ocean with a wind speed of 7 m $s^{-1}$ at 10 m. Figure 8 shows the simulated radiances for the spherical and non-spherical models as a function of the optical thickness for a given geometry . The arrows illustrate the error which would be made in the AOT inversion if the spherical model was used. Note that, in this particular case, the error caused by the lack of knowledge of the aerosol model increases with AOT. In a more realistic case, errors would also be due to uncertainties in the aerosol vertical profile, aerosol refractive index, and surface representation. Thus single-view sensors are prone to large errors in estimating the AOT in the case of non-spherical aerosols. However, multi-angular sensors, such as POLDER or MISR (Kahn *et al.* 1997), are capable of detecting aerosol non-sphericity.

### (*d*) *Impact of erroneous AOT on the DARP*

Errors made on the AOT retrieval and DARP calculation are presented in Fig. 9 for three values of the SZA. Figure 9(a) shows the scattering angle, $\Theta$, and Fig. 9(b) the ratio between the retrieved spherical AOT and the given non-spherical AOT taken

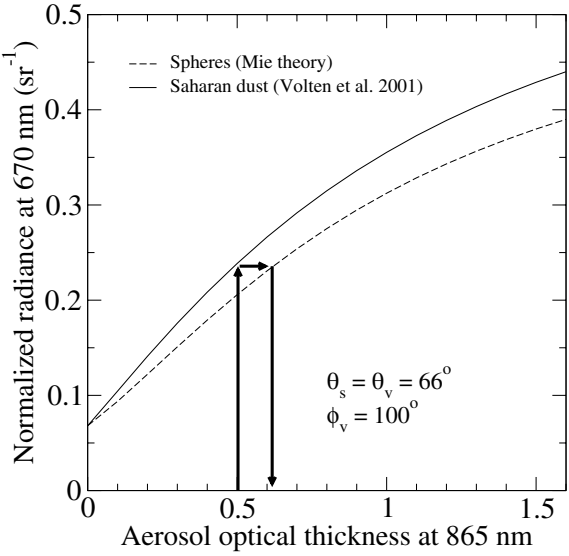


Figure 8. Simulated top-of-atmosphere normalized radiance at 670 nm as a function of aerosol optical thickness (AOT) for the non-spherical (solid line) and spherical (dashed line) aerosol models. (The geometry is defined by the view zenith angle, $\theta_v$, and the relative azimuthal angle, $\phi_v$, between the sun and the satellite.) If non-spherical aerosols are present in the atmosphere at an AOT of 0.5 (at 865 nm), inversion of the measured radiance assuming spherical aerosols would produce an optical thickness larger than 0.6.

at 0.1 at 865 nm. The DARP is then recomputed using the retrieved spherical AOT and compared to the DARP calculated using the given non-spherical AOT. Figure 9(c) shows the ratio between these two DARPs.

Some viewing geometries are more liable to errors than others. Very few geometries have a ratio of 1 between the non-spherical AOT and the retrieved spherical AOT. As a consequence, the recomputed DARP for spherical particles almost never equals the DARP for non-spherical aerosols. The ratios between the spherical and non-spherical cases do not follow the exact pattern of the scattering angles (compare Figs. 9(a) and (b)), so considering the full viewing geometry is mandatory. Polar diagrams exhibit a deep minimum around the backscatter area, where $\Theta$ approaches 180°, which corresponds to a $\phi_v$ of 180° when $\theta_s = \theta_v$. This minimum is surrounded by the contour 1, where spherical and non-spherical AOTs and DARPs are about the same. Then, in the wide area characterized by scattering angles between 80° and 140°, the spherical AOT and DARP are larger than their non-spherical counterparts, which translates into ratios reaching 1.6 and 1.3 at small and large non-spherical AOT, respectively.

Finally, in the forward-scattering area, where $\phi_v$ is less than 60° and at large view zenithal angle, ratios range between 0.8 and 1.2. In this region, when $\theta_v$ nearly equals the SZA, $\theta_s$, the spatial instrument looks directly into the sunglint. This particular viewing geometry is generally not used in the inversion, as the aerosol contribution to the total signal is overcome by the surface contribution. The general pattern remains the same with increasing non-spherical AOT (Figs. 9(d)–(f)). Errors made on the AOT are yet smaller in the $\Theta = 120°$ area.

The ratio between the retrieved spherical AOT and given non-spherical AOT is mainly driven by the differences in the phase functions (Fig. 6(a)). If the spherical aerosol phase function is larger than the non-spherical one, it takes smaller AOT to

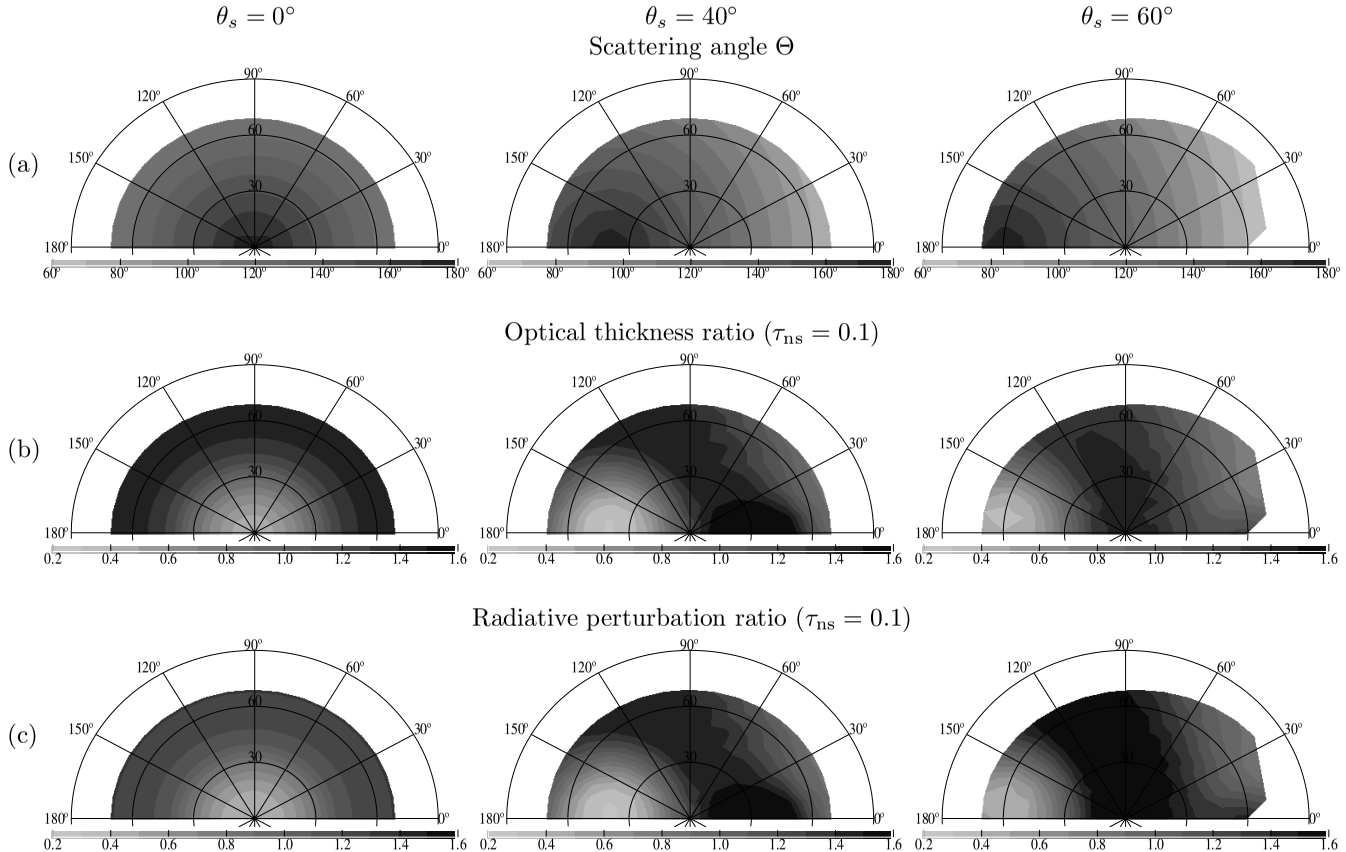


Figure 9. For three values of the solar zenith angle, $\theta_s$, polar diagrams showing (a) the scattering angle $\Theta$ (degrees), (b) the ratio between the retrieved spherical and non-spherical aerosol optical thicknesses for a non-spherical optical thickness, $\tau_{ns}$, of 0.1 (at 865 nm), (c) the ratio between the recomputed spherical and non-spherical DARP. (d) and (e) are as (b) and (c) respectively but for $\tau_{ns} = 0.4$. (f) is as (b) but for $\tau_{ns} = 1.0$. The radial axis is the view zenith angle, $\theta_v$, ranging from 0° (centre) to 90° (outer half-circle) and the azimuthal axis is the relative azimuthal angle, $\phi_v$, ranging from 0° (forward-scattering) to 180° (back-scattering). In these diagrams, the scattering angle is limited to 60° to 180°; smaller scattering angles have been removed as they are not reached by space sensors.

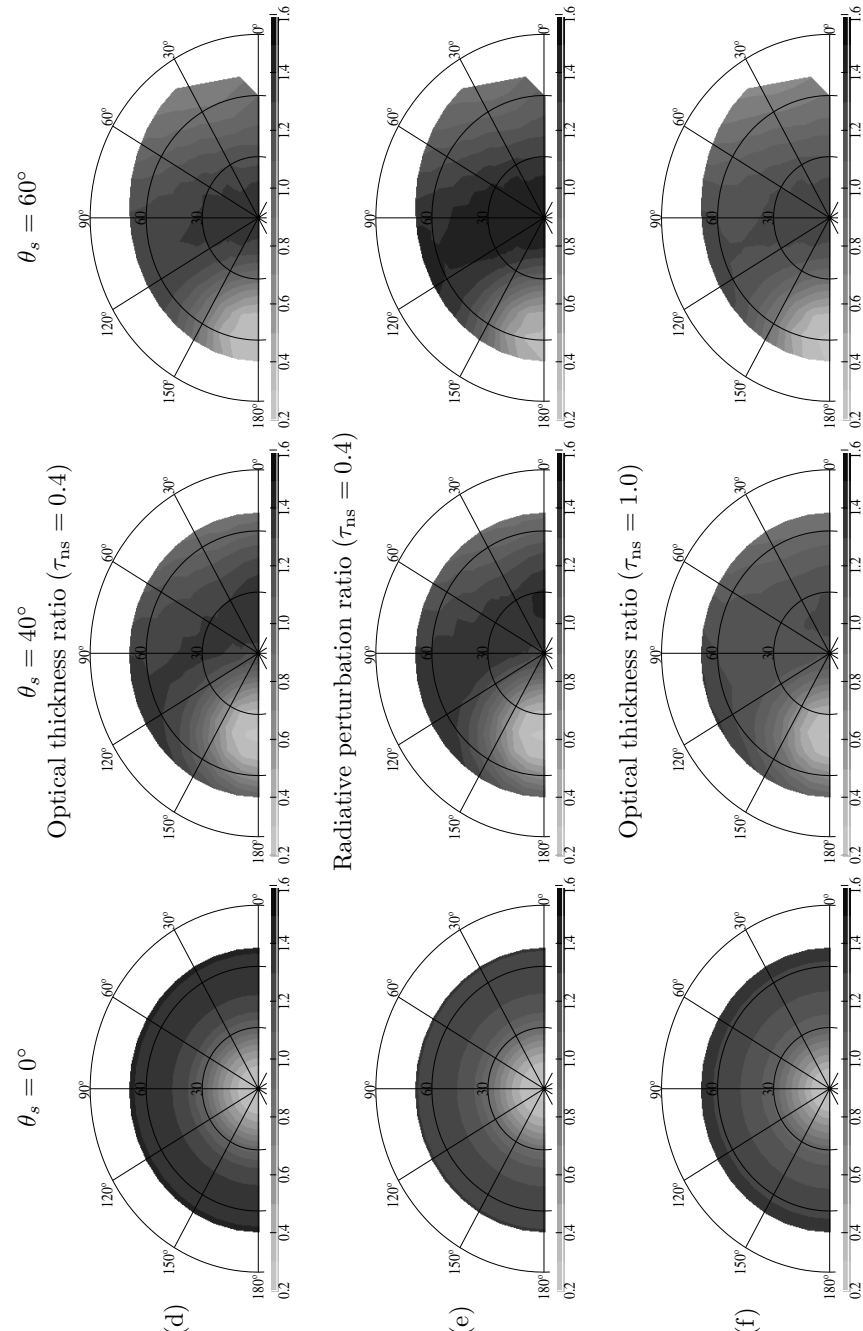


Figure 9. Continued.

fit the upward reflectance induced by the non-spherical particles. This is the case in the backscatter area, for instance. On the contrary, when the spherical aerosol phase function is smaller, then larger AOT are needed. This is the case at sidescattering angles. Of course, when both phase functions are comparable, retrieved spherical AOT nearly equals the given non-spherical one. This can be seen on isoline 1, which roughly matches the $\Theta = 80°$ and 150° isolines. When the given non-spherical AOT is increased to 0.4 and 1.0, the spherical AOT gets closer to the non-spherical one at scattering angles outside the backscatter region. This effect is particularly strong at sidescattering angles, and is due to multiple scattering. As photons are scattered by several particles, their scattering angles cover a large range, thus involving the whole phase function. As both aerosol models have similar asymmetry parameters, this lessens the importance of specific differences between spherical and non-spherical phase functions.

Errors made on the DARP do not match those made on the AOT. Their interpretation involves the upscatter fraction, $\beta(\theta_s)$, presented in Fig. 6(b). The three values used for the SZA correspond to three different cases. When $\theta_s = 0°$ ($\cos\ \theta_s = 1.0$), the upscatter fraction of the spherical aerosols is smaller than for the non-spherical case. It is nearly equal at $\theta_s = 40°$ ($\cos\ \theta_s = 0.77$), and larger at $\theta_s = 60°$ ($\cos\ \theta_s = 0.5$). For $\theta_s = 0°$, there is a compensation between errors on the AOT and on the DARP for sidescattering angles. Retrieved spherical AOTs are indeed larger than given non-spherical ones in this area, but there is also less upscatter at this SZA. On the contrary, when $\Theta = 180°$, the AOT is underestimated and the depreciated upscatter amplifies the errors. This is the exact opposite of when $\theta_s = 60°$, with a larger spherical upscatter. When $\theta_s = 40°$, the upscatter fractions are the same for spherical and non-spherical particles. In this case, the errors on the retrieved AOTs are simply transferred to the computed DARP, without any compensation or amplification.

## 4. Conclusion

We have presented radiative transfer simulations assessing the impact on the DARP of two widely-used, simplifying hypotheses—using a Lambertian albedo to represent the surface, and neglecting the effects of aerosol non-sphericity. Using a radiative transfer code able to model the surface through either its Lambertian albedo or its BRDF, we found that the surface albedo of the open ocean is strongly dependent on the AOT, especially at large SZAs, where an AOT of 0.1 at 865 nm decreases the albedo by almost one third. If this dependence is taken into account, errors due to the use of the albedo instead of the BRDF are very small, and the dependence of the DARP with SZA is well reproduced. If the prescribed albedo does not depend on the aerosol loading, relative errors made on the DARP can reach 20% at small AOTs. Large AOTs are required to bring the errors to less than 10%. Errors are smaller for the daily-averaged DARP, except for northern hemisphere winter. Assigning different surface albedos to direct and diffuse radiation would be a simple and affordable way to mimic the surface BRDF behaviour in simplified radiative transfer codes, such as those used in general-circulation models of the atmosphere. The development of parametrizations for surface albedo as a function of spectral AOT for each aerosol model used could also be a suitable solution.

Spherical and non-spherical dust aerosols exhibit dissimilar phase functions and upscatter fractions. As a consequence, these differences in shapes leads to significant differences in the DARP. If the same AOT is used for both models, relative errors in the DARP can be as large as 15%, and only a daily integration is able to reduce the errors to acceptable values. If top-of-the-atmosphere upward radiances estimated from a non-spherical aerosol model are inverted using a spherical aerosol model, there can be large

errors in the AOT retrieval and the subsequent DARP estimation. We further showed that some viewing geometries are more prone to errors than others. Backscatter is very sensitive to aerosol non-sphericity effects whereas AOT inversion at sidescattering angles (120° to 140°) shows little dependence on aerosol shape. The impact of dust non-sphericity should nevertheless be considered in satellite and model estimates of the radiative impact of aerosols.

## ACKNOWLEDGEMENTS

Hester Volten is acknowledged for providing the non-spherical phase function. The Laboratoire d'Optique Atmosphérique is a member of the 'Fédération de recherche' of the Centre Nationale de la Recherche Scientifique (CNRS) FR1818. This study has been supported by the 'Programme National de Télédétection Spatiale' of the CNRS. Calculations were conducted on the high-performance computer of Lille University. This equipment was funded in part by the 'Fond Européen de Développement Régional' of the European Union.

## REFERENCES

Boucher, O. 1998 On aerosol direct shortwave forcing and the Henyey-Greenstein phase function. *J. Atmos. Sci.*, **55,** 128–134

Boucher, O., Schwartz, S. E., Ackerman, T. P., Anderson, T. L., Bergstrom, B., Bonnel, B., Chylek, P., Dahlback, A., Fouquart, Y., Fu, Q., Halthore, R. N., Haywood, J. M., Iversen, T., Kato, S., Kinne, S., Kirkevaag, A., Knapp, K. R., Lacis, A., Laszlo, I., Mishchenko, M. I., Nemesure, S., Ramaswamy, V., Roberts, D. L., Russell, P., Schlesinger, M. E., Stephens, G. L., Wagener, R., Wang, M., Wong, J. and Yang, F. 1998 Intercomparison of models representing direct shortwave radiative forcing by sulfate aerosols. *J. Geophys. Res.*, **103,** 16979–16998

Charlson, R. J., Schwartz, S. E., Hales, J. M., Cess, R. D., Coakley, J. A., Hansen, J. E. and Hofmann, D. J. 1992 Climate forcing by anthropogenic aerosols. *Science*, **255,** 423–430

Chylek, P. and Wong, J. 1995 Effect of absorbing aerosols on global radiation budget. *Geophys. Res. Lett.*, **22,** 929–931

Cox, C. and Munk, W. 1954 Measurement of the roughness of the sea surface from photographs of the Sun's glitter. *J. Opt. Soc. Am.*, **44,** 838–850

Deuzé, J.-L., Goloub, P., Herman, M., Marchand, A., Perry, G., Susana, S. and Tanré, D. 2000 Estimate of the aerosol properties over the ocean with POLDER. *J. Geophys. Res.*, **105,** 15329–15346

Dubovik, O. B., Holben, B., Eck, T. F., Smirnov, A., Kaufman, Y. J., King, M. D., Tanré, D. and Slutsker, I. 2002 Variability of absorption and optical properties of key aerosol types observed in worldwide locations. *J. Atmos. Sci.*, **59,** 590–608

Haywood, J. M. and Shine, K. P. 1995 The effect of anthropogenic sulfate and soot aerosol on the clear sky planetary radiation budget. *Geophys. Res. Lett.*, **22,** 602–606

Haywood, J. M., Francis, P., Osborne, S., Glew, M., Loeb, N., Highwood, E., Tanré, D., Myhre, G. and Formenti, P. 2003 Radiative properties and direct radiative effect of Saharan dust measured by the C-130 aircraft during SHADE: 1. Solar spectrum. *J. Geophys. Res.*, **108,** 8577, doi: 10.1029/2002JD002687

Kahn. R., West, R., McDonald, D., Rheingans, B. and Mishchenko, M. I. 1997 Sensitivity of multiangle remote sensing observations to aerosol sphericity. *J. Geophys. Res.*, **102,** 16861–16870

Key, J. R. and Schweiger, A. J. 1998 Tools for atmospheric radiative transfer: STREAMER and FLUXNET. *Computers & Geosciences*, **24,** 443–451

Mishchenko, M. I., Lacis, A. A., Carlson, B. E. and Travis, L. D. 1995 Nonsphericity of dust-like tropospheric aerosols: implications for aerosol remote sensing and climate modeling. *Geophys. Res. Lett.*, **22,** 1077–1080

Mishchenko, M. I., Travis, L. D. and Mackowski, D. W. 1996 T-Matrix computations of light-scattering by nonspherical particles: A review. *J. Quant. Spectrosc. Radiat. Transfer*, **55,** 535–575

Mishchenko, M. I., Travis, L. D., Kahn, R. A. and West, R. A. 1997 Modeling phase functions for dustlike tropospheric aerosols using a shape mixture of randomly oriented polydisperse spheroids. *J. Geophys. Res.*, **102,** 16831–16847

Mugnai, A. and Wiscombe, W. J. 1986 Scattering from nonspherical Chebyshev particles. I: Cross sections, single-scattering albedo, asymmetry factor, and backscattered fraction. *Appl. Opt.*, **25,** 1235–1244

1989 Scattering from nonspherical Chebyshev particles. III: Variability in angular scattering patterns. *Appl. Opt.*, **28,** 3061–3073

Nemesure, S., Wagener, R. and Schwartz, S. E. 1995 Direct shortwave forcing of climate by anthropogenic sulfate aerosol: Sensitivity to particle size, composition and relative humidity. *J. Geophys. Res.*, **100,** 26105–26116

Pilinis, C. and Li, X. 1998 Particle shape and internal inhomogeneity effects on the optical properties of tropospheric aerosols of relevance to climate forcing. *J. Geophys. Res.*, **103,** 3789–3800

Russell, P. B., Kinne, S. A. and Bergstrom, R. W. 1997 Aerosol climate effects: Local radiative forcing and column closure experiment. *J. Geophys. Res.*, **102,** 9397–9407

Stamnes, K., Tsay, S., Wiscombe, W. and Jayaweera, K. 1988 Numerically stable algorithm for discrete-ordinate-method radiative transfer in multiple scattering and emitting layered media. *Appl. Opt.*, **27,** 2502–2509

Tanré, D., Herman, M. and Deschamps, P.-Y. 1983 Influence of the atmosphere on space measurements of directional properties. *Appl. Opt.*, **21,** 733–741

Volten, H., Muñoz, O., Rol, E., de Haan, J. F., Vassen, W. and Hovenier, J. W. 2001 Scattering matrices of mineral aerosol particles at 441.6 nm and 632.8 nm. *J. Geophys. Res.*, **106,** 17375–17401

Wang, J., Liu, X., Christopher, S., Reid, J., Reid, E. and Maring, H. 2003 The effect of non-sphericity on geostationary satellite retrievals of dust aerosols. *Geophys. Res. Lett.*, **30,** 2293, doi: 10.1029/2003GL018697

Wiscombe, W. J. and Grams, G. W. 1976 The backscattered fraction in two-stream approximations. *J. Atmos. Sci.*, **33,** 2440-2451

Wiscombe, W. J. and Mugnai, A. 1988 Scattering from nonspherical Chebyshev particles. II: Means of angular scattering patterns. *Appl. Opt.*, **27,** 2405–2421

Yang, P., Liou, K. N., Mishchenko, M. I. and Gao, B 2000 Efficient finite-difference time-domain scheme for light-scattering by dielectric particles: application to aerosols. *Appl. Opt.*, **39,** 3727–3737

Zhao, T., Laszlo, I., Dubovik, O., Holben, B., Sapper, J., Tanré, D. and Pietras, C. 2003 A study of the effect of non-spherical dust particles on the AVHRR aerosol optical thickness retrievals. *Geophys. Res. Lett.*, **30,** 1317, doi: 10.1029/2002GL016379